ORIGINAL ARTICLE

Three-phase flying-capacitor MMC with six coupled inductors

Duc Dung Le[1] · **Dong-Choon Lee**[1] · **Heung-Geun Kim**[2]

Abstract

In this paper, the design and integration of coupled inductors have been proposed for a flying-capacitor (FC) modular multilevel converter (MMC) for induction motor drive applications. In the conventional three-phase FC-MMC, twelve discrete inductors are needed for three legs. However, by integrating one coupled inductor with two windings in two half-arms, the number of inductors required is reduced from 12 to 6. Accordingly, the overall volumes and weights of cores and windings can be reduced by 41.7% and 41.4% when compared with discrete inductors. To confirm the validity of the proposed coupled inductor, a 4160-V/1-MW simulation model of a FC-MMC and a 220-V/3-kW scaled-down prototype have been built, of which performance for induction motor drives has been tested from standstill to the rated speed.

Keywords Coupled inductor · Flying-capacitor modular multilevel converters (FC-MMC) · Medium-voltage motor drives · Submodule (SM) capacitor · Voltage ripple

1 Introduction

In the past decade, modular multilevel converters (MMC) has attracted a great deal of interest in the medium and high-voltage applications. For high-voltage direct-current (HVDC) transmission, MMC-based HVDC systems have been installed in San Francisco's Trans Bay, INELEF and Sydvastlanken [1, 2, 11, 3–10]. In addition, MMC is able to operate as static synchronous compensators (STATCOMs) to compensate both harmonics and reactive power [12, 13]. Another potential application for MMCs is medium-voltage AC motor drives [14–17]. There are also a number of commercial products in terms of MMC-based motor drive systems such as Sinamics SM120 and M2L 3000 [18, 19]. MMC has several favorable features such as modularity, scalability, high capacity and low harmonic voltage content. In spite of these advantages, one of the main challenges of MMC is submodule (SM) capacitor voltage ripples under the low-speed operation of motor drives, where the magnitude is in proportion to the output current level and in inverse

proportion to the phase frequency [17]. Hence, the performance of MMC at low output frequency is deteriorated.

This issue can be alleviated by injecting high-frequency common-mode voltage (CMV) [17]. However, the injected CMV is imposed on the motor winding, which can eventually lead to the deterioration of motor winding insulation and motor bearing. As another solution to suppress SM capacitor voltage ripples without deteriorating the motor winding, a flying-capacitor modular multilevel converter (FC-MMC) has been suggested for medium-voltage AC motor drives [20]. In the FC-MMC, each phase leg is equipped with a flying capacitor which links the conjunction nodes of both arms. During low-speed operation, the injected high-frequency voltage produces a high-frequency circulating current. This current is utilized to redistribute the power imbalance between the upper and lower arms through the flying capacitor. Therefore, it is noted that the FC-MMC can be applied over the entire speed range from standstill to the rated speed.

However, in the FC-MMC, one discrete inductor is assembled in each half-arm to minimize the inrush current and to obtain a stable control performance of the high-frequency circulating current. Thus, twelve discrete inductors are employed, which are bulky and heavy. One feasible measure to reduce the volume and weight of the inductor is a magnetic integration scheme.

✉ Dong-Choon Lee
dclee@yu.ac.kr

[1] Department of Electrical Engineering, Yeungnam University, Gyeongsan, South Korea

[2] Department of Electrical Engineering, Kyungpook National University, Daegu, South Korea

Coupled inductors have been employed in a wide variety of converters such as grid-connected inverters, interleaved converters, triple-star bridge-cells converters, and MMCs [3, 21–27]. In grid-connected inverters, coupled inductors have been utilized in the LCL and LLCL filters [21, 22]. This significantly reduces the volume and weight of the magnetic component and effectively attenuates the switching harmonics. In addition, magnetic integration in the interleaved multiphase converter makes it more compact compared with discrete inductors [23]. The coupled inductor has also been discussed for triple-star bridge-cells converters to save core and coil materials [24, 25]. In the conventional MMC, the advantages of a coupled inductor have been utilized [3, 26, 27]. It was shown that the THD of the output voltage can be improved by increasing the differential-mode inductance of the coupled inductor [26]. In addition, the integrated inductor is designed based on the effective inductance for the circulating current of the converter [3, 27]. For the FC-MMC, however, the utilization of coupled inductors has not been applied.

This paper proposes an integration scheme of coupled inductors in a FC-MMC, which is expanded from [28]. By assembling the positive and negative coupled inductors in the upper and lower arms, respectively, the impedance of an LC circuit is kept as the lowest value. In addition, a magnetic design and dimension comparison of the inductors are described, from which it is demonstrated that the coupled inductors are 41.7% smaller in volume and 41.4% lighter in weight when compared with discrete inductors. Finally, to confirm the operation of the coupled inductor strategy for the FC-MMC, a 4160-V/1-MW simulation model and a 220-V/3-kW scaled-down prototype are built and tested over the full speed operating range of induction motor drives.

2 Flying-capacitor MMC

2.1 Circuit structure

Figure 1 illustrates the circuit structure of the FC-MMC that is comprised of three legs. A leg consists of two arms (an upper arm and a lower arm). The number of half-bridge SMs per arm is N_{SM} and an arm is separated into two half-arms. In addition, one inductor per half-arm is added and a flying capacitor is used to link the middle conjunction nodes of the upper and lower arms. The flying capacitance, C_F, is given by

$$C_F = \frac{1}{(2\pi f_h)^2 L},\tag{1}$$

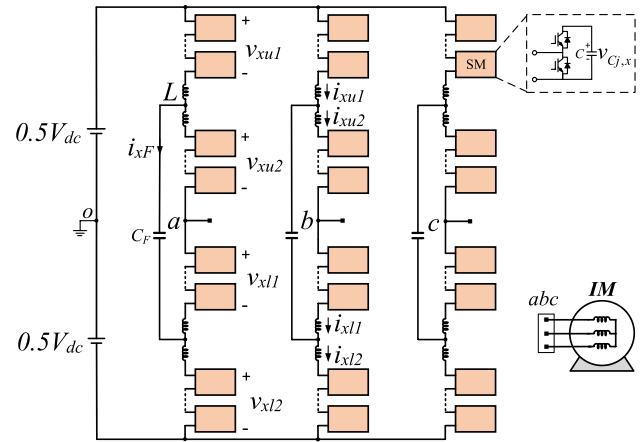where f_h and L are the injected frequency and the half-arm inductance, respectively [20].
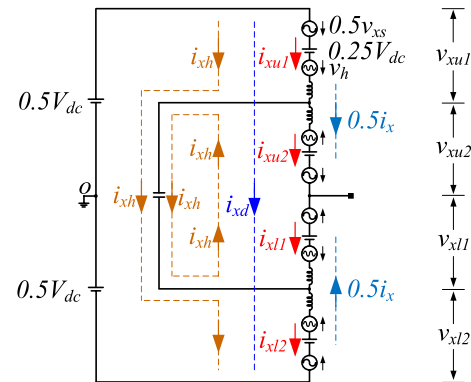

Fig. 1 Circuit structure of the FC-MMC

Fig. 2 Per-phase equivalent circuit of a leg

2.2 Basic operating principle

A per-phase equivalent circuit of a leg is shown in Fig. 2, where the half-arm voltages and currents consist of the DC, fundamental frequency and high-frequency components. The voltages of the four half-arms (v_{xu1}, v_{xu2}, v_{xl1} and v_{xl2}) are expressed as

$$v_{xu1} = 0.25V_{dc} - 0.5v_{xs} - v_h,\tag{2}$$

$$v_{xu2} = 0.25V_{dc} - 0.5v_{xs} + v_h,\tag{3}$$

$$v_{xl1} = 0.25V_{dc} + 0.5v_{xs} - v_h,\tag{4}$$

$$v_{xl2} = 0.25V_{dc} + 0.5v_{xs} + v_h,\tag{5}$$

where V_{dc}, v_{xs} and v_h are the DC-link voltage, phase voltage and high-frequency voltage, respectively. In addition, the half-arm currents (i_{xu1}, i_{xu2}, i_{xl1} and i_{xl2}) are given as

$$i_{xu1} = i_{xd} + 0.5i_x + i_{xh}, \tag{6}$$

$$i_{xu2} = i_{xd} + 0.5i_x - i_{xh}, \tag{7}$$

$$i_{xl1} = i_{xd} - 0.5i_x - i_{xh}, \tag{8}$$

$$i_{xl2} = i_{xd} - 0.5i_x + i_{xh}, \tag{9}$$

where i_{xd}, i_x and i_{xh} are the DC component of the circulating current flowing in the leg, AC output current and high-frequency circulating current component, respectively. During low-speed operation, the power imbalance between the upper and lower arms is redistributed through the flying capacitor by the high-frequency circulating current, i_{xh}. Since the constant power of the interaction of v_h and i_{xh} can alleviate low-frequency power fluctuations, the instantaneous power absorbed by the half-arms includes only high-frequency power component. Therefore, current flows through the SM capacitors at high frequency, which leads to a significant reduction in the SM capacitor voltage ripples [20].

3 Design of arm inductors

As demonstrated in Fig. 2, a half-arm conducts the DC and AC circulating current components (i_{xd} and i_{xh}) additional to the output current (i_x). In a leg, the DC circulating current, i_{xd}, is equal to one-third of the DC input current, which is used to control the average voltage of a leg to follow the SM voltage reference, v_c^*. The high-frequency circulating current, i_{xh}, of the top half-arm flows in the opposite direction to that of the bottom half-arm, which redistributes the power imbalance through the flying capacitor, C_F. Besides, the sum of the high-frequency circulating currents is zero ($i_{ah} + i_{bh} + i_{ch} = 0$). Thus, there is no influence of i_{xh} on the DC input or AC output currents of the converter.

To design the magnetic component, the effective inductances of the DC and high-frequency circulating currents (L_{xd} and L_{xh}) are taken into account to prevent high di/dt. The effective inductance for the output current (L_x) can be neglected due to the leakage inductances of the induction motor itself.

3.1 Discrete inductors

Figure 3 shows a schematic representation of the discrete inductor, which is used in a half-arm. The inductor voltage, $v_{Lxu/lk}$ ($k = 1, 2$), is expressed as
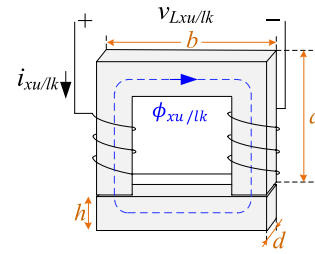

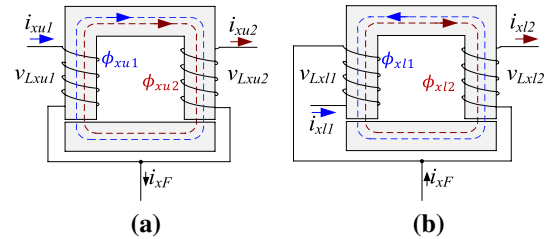**Fig. 3** Schematic representation of a discrete inductor

Fig. 4 Schematic representation of coupled inductors: **a** positive coupling; **b** negative coupling

$$\begin{aligned} v_{Lxu/lk} &= N\frac{\mathrm{d}\phi_{xu/lk}}{\mathrm{d}t} = \frac{N^2}{R}\frac{\mathrm{d}i_{xu/lk}}{\mathrm{d}t} \\ &= \frac{N^2}{R}\frac{\mathrm{d}}{\mathrm{d}t}(i_{xd} \pm 0.5i_x \pm i_{xh}), \end{aligned} \tag{10}$$

where N is the turns number and R is the magnetic reluctance including the air gap. The self-inductance is determined as

$$L = \frac{N^2}{R}. \tag{11}$$

From (10), the effective inductances for the DC circulating current, L_{xd_dis}, and the high-frequency circulating current, L_{xh_dis}, can be calculated as

$$L_{xd\_dis} = L_{xh\_dis} = L = \frac{N^2}{R}. \tag{12}$$

3.2 Coupled inductors

Figure 4a, b illustrate schematic representations of positive and negative coupled inductors, which are assembled in the upper and lower arms, respectively. Firstly, in the upper arm, the positive coupled inductor is taken into consideration. The inductor voltage in the top half-arm, v_{Lxu1}, is expressed as

$$v_{Lxu1} = L_{u1}\frac{\mathrm{d}i_{xu1}}{\mathrm{d}t} + M_{u2u1}\frac{\mathrm{d}i_{xu2}}{\mathrm{d}t}, \tag{13}$$

where L_{u1} is the self-inductance for coil u_1, and M_{u2u1} is the mutual inductance between coil u_2 and coil u_1. It is assumed that there is no leakage flux. Thus, L_{u1} and M_{u2u1} are calculated as

$$L_{u1} = \frac{N\phi_{xu1}}{i_{xu1}} = \frac{N}{i_{xu1}}\frac{Ni_{xu1}}{R} = \frac{N^2}{R}, \tag{14}$$

$$M_{u2u1} = \frac{N\phi_{xu2}}{i_{xu2}} = \frac{N}{i_{xu2}}\frac{Ni_{xu2}}{R} = \frac{N^2}{R}. \tag{15}$$

Substituting (6), (7), (14) and (15) into (13) yields

$$v_{Lxu1} = \frac{2N^2}{R}\frac{d(i_{xd} + 0.5i_x)}{dt}. \tag{16}$$

Similarly, the inductor voltage in the bottom half-arm, v_{Lxu2}, is equal to v_{Lxu1}. Therefore, the effective inductance for the DC circulating current, L_{xd_cou}, is calculated as

$$L_{xd\_cou} = \frac{2N^2}{R}. \tag{17}$$

Figure 5a shows an equivalent circuit with an effective inductance for the DC circulating current, where L_{xd_cou} is introduced in the upper arm. In addition, the value of inductance L_{xd_cou} is double the self-inductance in (14). Thus, the total effective inductance, through which the DC circulating current flows, is similar to that of in the FC-MMC with discrete inductors.

Next, the negative coupled inductor in the lower arm is analyzed. The inductor voltages in the top and bottom half-arms (v_{Lxl1} and v_{Lxl2}) are expressed, respectively, as

$$\begin{aligned}v_{Lxl1} &= L_{l1}\frac{di_{xl1}}{dt} - M_{l2l1}\frac{di_{xl2}}{dt}\\ &= -\frac{2N^2}{R}\frac{di_{xh}}{dt},\end{aligned} \tag{18}$$
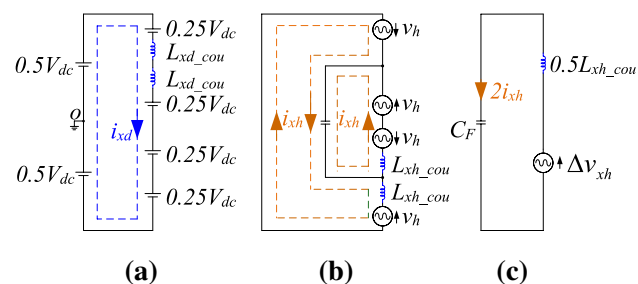

Fig. 5 Equivalent circuit of single-phase FC-MMC with coupled inductors: **a** equivalent circuit with an effective inductance applied to DC circulating current; **b** equivalent circuit with an effective inductance applied to high-frequency circulating current; **c** simplified circuit

$$v_{Lxl2} = \frac{2N^2}{R}\frac{di_{xh}}{dt}, \tag{19}$$

where L_{l1} is the self-inductance for coil l_1, and M_{l2l1} is the mutual inductance between coil l_2 and coil l_1. Thus, the effective inductance for the high-frequency circulating current, L_{xh_cou}, is calculated as

$$L_{xh\_cou} = \frac{2N^2}{R}. \tag{20}$$

Figure 5b shows a high-frequency equivalent circuit, where L_{xh_cou} is introduced in the lower arm. Then, a simplified circuit is illustrated in Fig. 5c, where it consists of an inductor, $0.5L_{xh\_cou}$, and the flying capacitor, C_F. Note that the inductance value of L_{xh_cou}, through which the high-frequency circulating current, i_{xh}, flows, is double the self-inductance in (14). As a result, the capacitance value of C_F is equal to that of the conventional FC-MMC, as mentioned in (1), in spite of the integration of coupled inductors.

3.3 Magnetic design and comparison

As shown in Fig. 2, the half-arm currents mainly include the frequency components of f_o and $f_o \pm f_h$, where f_o and f_h represent the fundamental and injected frequency components, respectively. It should be noted that the operating frequency range of f_o is $0 \sim 60$ Hz, whereas the injected frequency ($f_h = 100 \sim 200$ Hz) should be less than one-tenth of the switching frequency to obtain stable operation.

To compare the dimensions of discrete and coupled inductors, the parameters for the scaled-down prototype are selected. The effective inductance for the DC and high-frequency circulating current components is 2 mH in a half-arm. Besides, the maximum DC circulating current $i_{xd\_max} = 4$ A, the maximum output current $i_{x\_max} = 17$ A, and the maximum high-frequency circulating current $i_{xh\_max} = 20$ A are considered for the inductor design.

The core material for both the discrete and coupled inductor types is silicon steel. In addition, a rectangular wire with an AIW coating is selected for the windings. The number of winding turns is calculated as

$$N = \frac{\phi_{max}R}{I_{max}} = \frac{B_{max}A_cR}{I_{max}}, \tag{21}$$

where B_{max} is the maximum magnetic-flux density and A_c is the cross-sectional area of the core. The maximum current, I_{max}, is obtained from a superposition of the maximum values of the DC circulating current, I_{xd}, the output current, I_x, and the high-frequency circulating current, I_{xh}. Thus, in the case of the discrete inductor, the maximum current I_{max_dis} is 32.5 A ($I_{max\_dis} = I_{xd\_max} + 0.5I_{x\_max} + I_{xh\_max}$). Meanwhile, in the case of the coupled inductor, the maximum

Table 1 Comparison of dimensions and weights of inductors

Parameter	Discrete inductor	Coupled inductor
Coil turns (N)	88	64
a (cm)	8	10
b (cm)	6	6
d (cm)	5	5
h (cm)	2	2
I_{max} (A)	32.5	20
Total volume of core and winding (cm^3)	626	366
Total weight of core and winding (kg)	4.97	2.91

Table 2 Converter parameters and ratings

Parameter	Symbols	Simulation	Experiment
DC-link voltage	V_{dc}	7000 V	300 V
Half-arm inductance	L	2 mH	2 mH
Number of SMs per arm	N_{SM}	4	4
SM capacitance	C	3500 μF	2700 μF
Flying capacitance	C_F	1000 μF	1000 μF
SM capacitor voltage reference	v_c^*	1750 V	75 V
Carrier frequency	f_c	2000 Hz	2000 Hz
Injected high frequency	f_h	112.5 Hz	112.5 Hz

Table 3 Motor parameters and ratings

Parameter	Symbols	Simulation	Experiment
Output power	P_o	1250 hp	4 hp
Rated voltage	V_{LL}	4160 V	220 V
Rated current	I_{rated}	150 A	10.9 A
Rated frequency	f_o	60 Hz	50 Hz
Rated speed	ω_{rm_rated}	1189 rpm	1430 rpm
Rated torque	T_{rated}	7490 N.m	19 N.m

currents for the positive and negative couplings are 12.5 A ($I_{max\_pocou} = I_{xd\_max} + 0.5 I_{x\_max}$) and 20 A ($I_{max\_necou} = I_{xh\_max}$), respectively. By substituting (12) into (21), the number of winding turns in the discrete inductor is obtained as

$$N = \frac{I_{max}L}{A_c B_{max}}, \tag{22}$$

where $L = L_{xd\_dis} = L_{xh\_dis} = 2$ mH.

For the coupled inductor, substituting (17) and (20) into (21) yields

$$N = \frac{I_{max}L_{xd\_cou}}{2A_c B_{max}} = \frac{I_{max}L_{xh\_cou}}{2A_c B_{max}}, \tag{23}$$

where $L_{xd\_cou} = L_{xh\_cou} = 4$ mH. In addition, the design parameters of the positive and negative coupled inductors are considered to be the same due to the modular property of the converter.

A comparison of the dimensions and weights between two types of inductors is demonstrated in Table 1. It is concluded that the volume and weight reductions of the magnetic cores and the winding of the coupled inductor are around 41.7% and 41.4%, respectively, compared with discrete inductors. The numerical design of the inductor is described in the "Appendix".

4 Simulation results

To verify the operation of the proposed coupled inductor, a 4160-V/1-MW FC-MMC system with 24 SMs has been modeled for simulation. The circuit parameters and ratings of the MMC and the induction motor are listed in Tables 2 and 3, respectively.

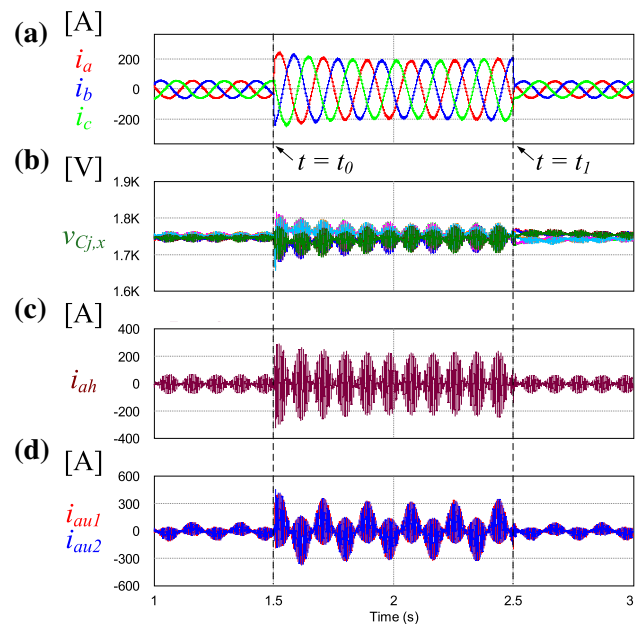Figure 6 illustrates shows the performance of an FC-MMC with coupled inductors at low-speed operation

Fig. 6 Performance at low-speed operation ($\omega_{rm} = 100$ rpm) under load changes: **a** three-phase output currents; **b** SM capacitor voltages; **c** high-frequency circulating current; **d** top and bottom half-arm currents in the upper arm

($\omega_{rm} = 100$ rpm) when the load torque is changed from no load to full load and back to no load at $t = t_0$ and $t = t_1$,

respectively. Figure 6a shows the three-phase output currents (i_a, i_b and i_c), where they are well balanced in both the transient and steady states. In addition, the fundamental frequency of the output current is 5 Hz. The SM capacitor voltages are demonstrated in Fig. 6b, where they are well controlled to follow the reference v_c^* (1750 V). Figure 6c shows the high-frequency circulating current, i_{ah}, which includes 112.5 Hz of the injected frequency component, f_h, and 5 Hz of the fundamental component, f_o. In addition, the half-arm currents (i_{au1} and i_{au2}) in the upper arm are shown in Fig. 6d. At full load, the amplitude of i_{xh} is increased to redistribute the power difference between the upper and lower arms, where the amplitudes of the half-arm currents are higher than those of the no-load condition.

Figure 7 shows inductor voltage waveforms in four half-arms, where v_{Lxu/lk_mes} is the measured voltage and v_{Lxu/lk_cal} is the calculated voltage from (16), (18) and (19). For the positive coupled inductor in the upper arm, Fig. 7a, b show the inductor voltages in the top and bottom half-arms ($v_{Lxu1} = v_{Lxu2}$), which include the low-frequency component (f_0) as mentioned in (16) and the switching frequency component. On the other hand, for the negative coupled inductor in the lower arm, Fig. 7c, d show the inductor voltages in the top and bottom half-arms ($v_{Lxl1} = -v_{Lxl2}$), which consist of the injected frequency component (f_h) as mentioned in (18) and (19).

Figure 8 illustrates the system performance of the accelerating process from zero to the rated speed under the no-load condition. The motor speed, ω_{rm}, which is accelerated from 0 to 1189 rpm, is shown in Fig. 8a. The line-to-line output voltage, v_{ab}, and the three-phase output currents (i_a, i_b and i_c) are shown in Fig. 8b, c, respectively, where

Fig. 8 Performance of the accelerating process from zero to the rated speed under no load condition: **a** motor speed; **b** line-to-line voltage; **c** three-phase output current; **d** SM capacitor voltages; **e** high-frequency circulating current; **f** flying capacitor voltage in phase-a

their fundamental frequency, f_o, is raised from zero to the rated frequency. The SM capacitor voltages are illustrated in Fig. 8d, where their ripples are initially high but within specified limits. After that, they are well controlled to follow the reference v_c^*. The high-frequency circulating current of phase-a is demonstrated in Fig. 8e, which is decreased as the motor speed is increased. Figure 8f illustrates the flying capacitor voltage of phase-a.

5 Experimental results

A small-scaled prototype of a three-phase FC-MMC with 24 SMs has been built, where six coupled inductors are integrated. Figure 9 shows the configuration of the experimental
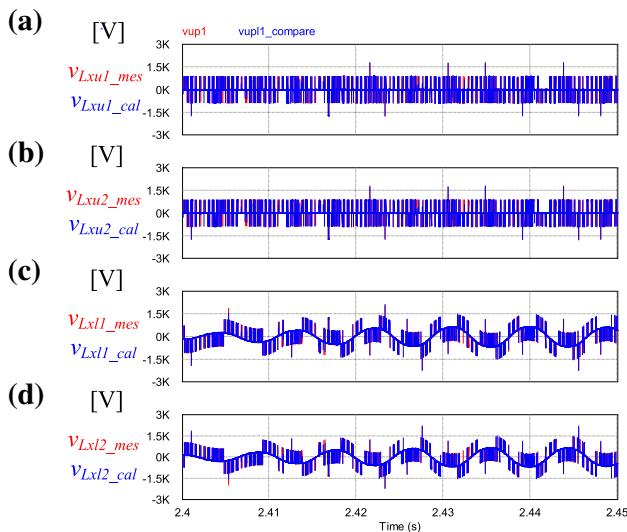

Fig. 7 Inductor voltage waveforms in four half-arms: **a** top half-arm in the upper arm; **b** bottom half-arm in the upper arm; **c** top half-arm in the lower arm; **d** bottom half-arm in the lower arm
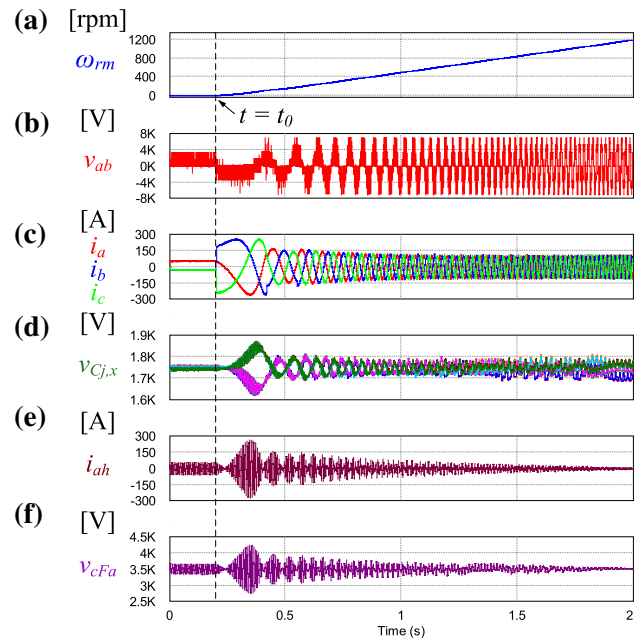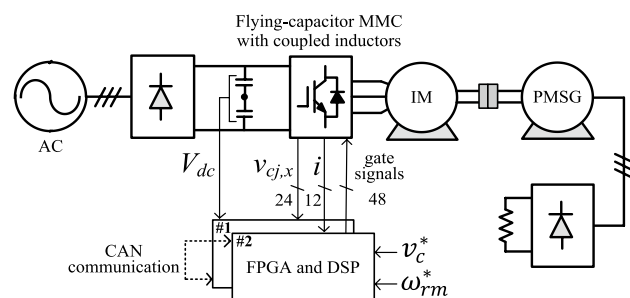

Fig. 9 Configuration of experimental system

system, where a 220-V/3-kW induction motor is mechanically coupled with a PMSG to apply a load. The specifications of the MMC and induction motor used for the experiment are given in Tables 2 and 3, respectively. Photographs of the FC-MMC prototype, and the inductors are shown in Figs. 10 and 11, respectively.

Figure 12 shows the performance at low-speed operation under load change conditions. A load torque is changed from no load to full load at $t = t_0$ and then back to no load at $t = t_1$. Figure 12a demonstrates shows the motor speed at $\omega_{rm} = 180$ rpm, where it follows well the reference under both the no load and full load conditions. The three-phase output currents (i_a, i_b and i_c) are illustrated in Fig. 12b. Magnifications of the output current at transient states are also shown in Fig. 12c with 10.9 A in the RMS value at a full load. The SM capacitor voltages of phase-a are shown in Fig. 12d, which are well controlled to follow the reference v_c^* (75 V). The high-frequency circulating current, i_{ah}, is illustrated in Fig. 12e, which is comprised of 112.5 Hz of the injected frequency component, f_h, additional to 6 Hz of the fundamental frequency component, f_o. At the full load condition, the amplitude of i_{ah} is increased to mitigate the SM capacitor voltage ripples. Figure 12f shows the half-arm currents (i_{au1} and i_{au2}) in the upper arm, which are also increased at the full load condition.

Figure 13 shows the performance of the acceleration operation at no load condition. The motor speed, ω_{rm}, is increased from zero at $t = t_0$ to the rated speed as shown in Fig. 13a. The line-to-line output voltage and the
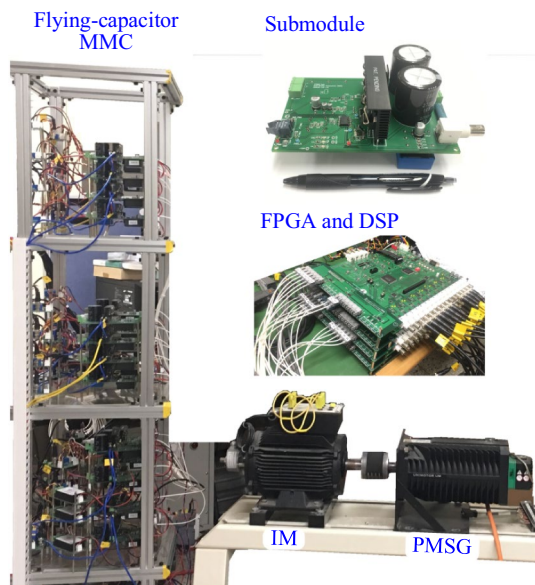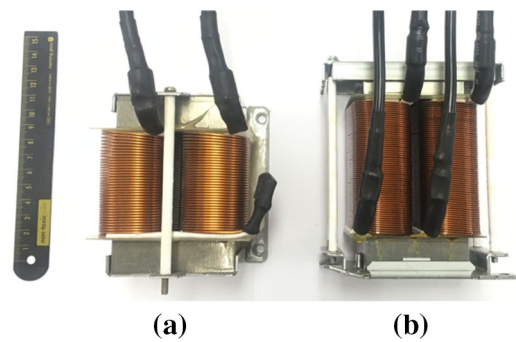

Fig. 11 Photographs of inductors: **a** discrete inductor; **b** coupled inductor

three-phase output current are illustrated in Fig. 13b, c, respectively. Figure 13d shows the performance of the high-frequency circulating current, i_{ah}. In the low-speed region, its amplitude is high owing to the requirement to balance the power difference between the upper and lower arms. On the other hand, in the high-speed region, the SM capacitor voltages are naturally balanced even without power redistribution between the upper and lower arms. Thus, the amplitude of i_{ah} becomes lower. The half-arm
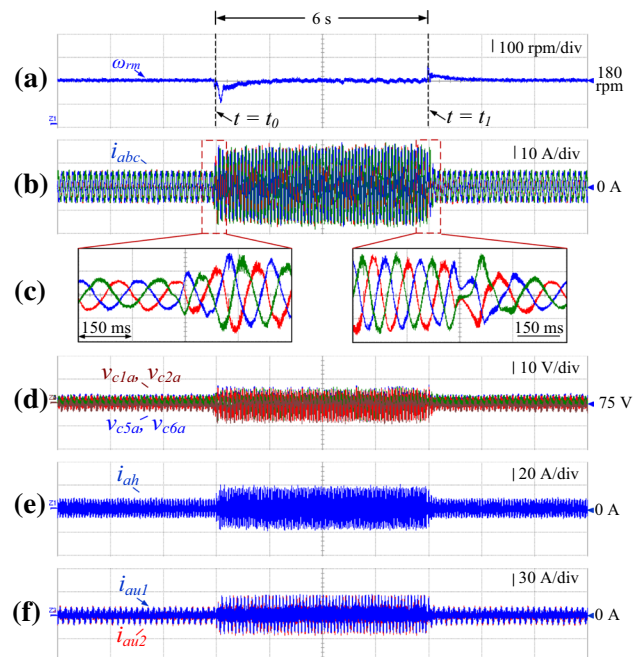

Fig. 12 Performance at low-speed operation ($\omega_{rm} = 180$ rpm) under load changes: **a** motor speed; **b** three-phase output current; **c** zoom-in of output current; **d** SM capacitor voltages of phase-a; **e** high-frequency circulating current; **f** top and bottom half-arm currents in the upper arm

Fig. 10 Prototype of a FC-MMC with coupled inductors for induction motor drives
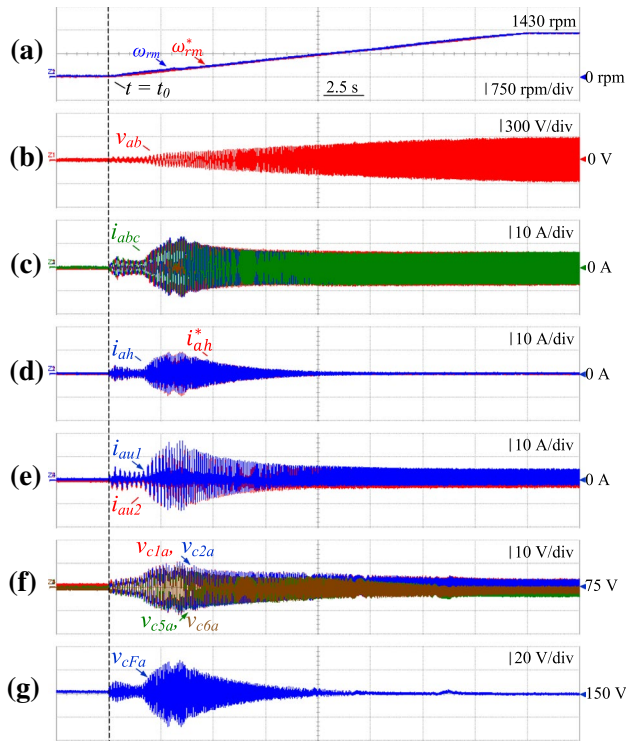
Fig. 13 Performance of the accelerating process from zero to the rated speed under no load condition: **a** motor speed; **b** line-to-line output voltage; **c** three-phase output current; **d** high-frequency circulating current; **e** top and bottom half-arm currents in the upper arm; **f** SM capacitor voltages of phase-*a*; **g** flying capacitor voltage in phase-*a*

currents in the upper arm and the SM capacitor voltages are shown in Fig. 13e, f, respectively. The flying capacitor voltage (v_{cFa}) is shown in Fig. 13g, where its ripple is low in the high-speed region.

6 Conclusions

In this paper, an integration scheme of the coupled inductors for an FC-MMC has been proposed to reduce the system volume and weight. With this concept, twelve discrete inductors can be reduced to six-coupled inductors. As a result, the volume and weight have been reduced by 41.7% and 41.4%, respectively. The validity of the FC-MMC with coupled inductors has been well proved by the simulation and experimental results for induction motor drive applications.

Appendix

Numerical design of the discrete and coupled inductors

As mentioned in section III, the self-inductances of the discrete and coupled inductors are 2 mH. In addition, the circuit parameters are listed in Tables 2 and 3. In [29], the area-product of the core, A_p, is expressed as

$$A_{\mathrm{P}} = \frac{S \times 10^4}{K_f K_u f_h B_{\max} J}, \tag{24}$$

where S, K_f, K_u and J are the apparent power, waveform factor, window utilization factor and current density of the winding (Table 4). Hence, the A_{P} of the discrete and coupled inductors is calculated as 115.3 cm^4 and 151 cm^4, respectively. Then, the cross-sectional area, A_c, and core window area, A_w, of the discrete inductor are selected as 10 cm^2 and 12 cm^2, respectively. For the coupled inductor, A_c and A_w are 10 cm^2 and 16 cm^2, respectively.

Next, in order to determine the wire size, the cross-sectional area of the copper winding, A_{cw}, is expressed as

$$A_{\mathrm{cw}} \geq \frac{I_{\mathrm{rms}}}{J}, \tag{25}$$

where I_{rms} of the discrete and coupled inductors is 23 A and 15 A, respectively. From this, A_{cw} is calculated as 7.36 mm^2 and 4.8 mm^2, respectively. According to the dimensional table of rectangular wire [30], the A_{cw} of the discrete inductor is selected as 7.5 mm^2, where the width and thickness are 0.75 cm and 0.1 cm, respectively. For the coupled inductor, A_{cw} is 4.8 mm^2. Thus, the width and thickness are 0.6 cm and 0.08 cm, respectively.

Finally, according to (22) and (23), the numbers of turns in the discrete and coupled inductors are calculated as 88 and 64, respectively. With the number of turns and the selected wire size, the core window area, A_w, needs to satisfy the following condition:

$$NA_{\mathrm{cw}} \leq K_u A_{\mathrm{w}}. \tag{26}$$

For the discrete inductor, 6.6 cm^2 < 7.2 cm^2, so the condition of (26) is satisfied. For the coupled inductor,

Table 4 Parameters used for inductor design

Parameter	Symbol	Value
Window utilization factor	K_u	0.6
Max. magnetic-flux density	$B_{\max}$	0.63 T
Silicon steel density	ρ_s	7.65 g/cm^3
Copper density	ρ_c	8.9 g/cm^3
Current density of winding	J	3.125 A/mm^2

$6.14\ \text{cm}^2 < 9.6\ \text{cm}^2$, thus, the conductor area fits the window area available in the selected cores.

References

1. Anupom, D., Shin, D.-C., Lee, D.-M.: Scheme for reducing harmonics in output voltage of modular multilevel converters with offset voltage injection. J. Power Electron. **19**(6), 1496–1504 (2019)
2. Debnath, S., Qin, J., Bahrani, B., Saeedifard, M., Barbosa, P.: Operation, control, and applications of the modular multilevel converter: a review. IEEE Trans. Power Electron. **30**(1), 37–53 (2015)
3. Hagiwara, M., Akagi, H.: Control and experiment of pulsewidth-modulated modular multilevel converters. IEEE Trans. Power Electron. **24**(7), 1737–1746 (2009)
4. Jo, Y.J., Nguyen, T.H., Lee, D.-C.: Capacitance estimation of the submodule capacitors in modular multilevel converters for HVDC applications. J. Power Electron. **16**(5), 1752–1762 (2016)
5. Lee, J.-M., Park, J.-W., Kang, D.-W., Lee, J.-P., Yoo, D.-W., Lee, J.-M.: Comparison of capacitor voltage balancing methods for 1GW MMC-HVDC based on real-time digital simulator and physical control systems. J. Power Electron. **19**(5), 1171–1181 (2019)
6. Zhang, J., Cui, D., Tian, X., Zhao, C.: Hybrid double direction blocking sub-module for MMC-HVDC design and control. J. Power Electron. **19**(6), 1486–1495 (2019)
7. Kim, C.-K., Belayneh, N.B., Park, C.-H., Kim, J.-M.: Maximum modulation index of VSC HVDC based on MMC considering compensation signals and AC network conditions. Trans. Korean Inst. Power Electron. **25**(1), 61–67 (2020)
8. Jo, K.-R., Seo, B.-J., Park, K.-S., Kim, H.-S., Heo, J.-Y., Nho, E.-C.: Performance test circuit and control method for submodule of MMC-HVDC system. Trans. Korean Inst. Power Electron. **24**(6), 452–458 (2019)
9. Nguyen, T.H., Al Hosani, K., El Moursi, M.S., Blaabjerg, F.: An overview of modular multilevel converters in HVDC transmission systems with STATCOM operation during pole-to-pole DC short circuits. Trans. Power Electron. **34**(5), 4137–4160 (2019)
10. Francos, P.L., Verdugo, S.S., Alvarez, H.F., Guyomarch, S., Loncle, J.: INELFE Europe's first integrated onshore HVDC interconnection. In: IEEE Power and Energy Society General Meeting, pp. 1–8 (2012)
11. Teeuwsen, S.P.: Modeling the trans bay cable project as voltage-sourced converter with modular multilevel converter design. In: IEEE Power and Energy Society General Meeting, pp. 1–8 (2011)
12. Ota, J.I.Y., Shibano, Y., Niimura, N., Akagi, H.: A phase-shifted-PWM D-STATCOM using a modular multilevel cascade converter (SSBC)—Part I: modeling, analysis, and design of current control. IEEE Trans. Ind. Appl. **51**(1), 279–288 (2015)
13. Ota, J.I.Y., Shibano, Y., Akagi, H.: A phase-shifted PWM D-STATCOM using a modular multilevel cascade converter (SSBC)—Part II: zero-voltage-ride-through capability. IEEE Trans. Ind. Appl. **51**(1), 289–296 (2015)
14. Dekka, A., Wu, B., Fuentes, R.L., Perez, M., Zargari, N.R.: "Evolution of topologies, modeling, control schemes, and applications of modular multilevel converters. IEEE J. Emerg. Sel. Top. Power Electron. **5**(4), 1631–1656 (2017)
15. Le, D.D., Lee, D.-C.: A modified hybrid modular multilevel converter with reduced capacitor voltage fluctuations and fault-tolerant operation ability. In: Proceedings of IEEE ECCE Asia, pp. 172–177 (2019)
16. Hagiwara, M., Hasegawa, I., Akagi, H.: Start-up and low-speed operation of an electric motor driven by a modular multilevel cascade inverter. IEEE Trans. Ind. Appl. **49**(4), 1556–1565 (2013)
17. Korn A.J.: Low output frequency operation of the modular multilevel converter. In: Proceedings of IEEE ECCE, pp. 3993–3997 (2010)
18. SIEMENS: Drives for every demand. https://cache.industry.siemens.com/dl/files/230/109746230/att_990809/v1/poster-SINAMICS-mv-drives_en.pdf (2019). Accessed 2 Nov 2019
19. BENSHAW: M2L Series M2L Medium Voltage Drive. https://www.benshaw.com/sites/default/files/downloads/brochures/benshaw-m2l-3000-brochure.pdf (2019). Accessed 5 Nov 2019
20. Du, S., Wu, B., Zargari, N.R., Cheng, Z.: A flying-capacitor modular multilevel converter for medium-voltage motor drive. IEEE Trans. Power Electron. **32**(3), 2081–2089 (2017)
21. Pan, D., Ruan, X., Bao, C., Li, W., Wang, X.: Magnetic integration of the LCL filter in grid-connected inverters. IEEE Trans. Power Electron. **29**(4), 1573–1578 (2014)
22. Fang, J., Li, H., Tang, Y.: A magnetic integrated LLCL filter for grid-connected voltage-source converters. IEEE Trans. Power Electron. **32**(3), 1725–1730 (2017)
23. Zumel, P., García, O., Cobos, J.A., Uceda, J.: Magnetic integration for interleaved converters. In: Proceedings of IEEE APEC, pp. 1143–1149 (2003)
24. Kawamura, W., Hagiwara, M., Akagi, H., Tsukakoshi, M., Nakamura, R., Kodama, S.: AC-inductors design for a modular multilevel TSBC converter, and performance of a low-speed high-torque motor drive using the converter. IEEE Trans. Ind. Appl. **53**(5), 4718–4729 (2017)
25. Kammerer, F., Kolb, J., Braun, M.: Optimization of the passive components of the modular multilevel matrix converter for drive applications. In: PCIM Europe conference proceedings, pp. 702–709 (2012)
26. Shi, X., Wang, Z., Tolbert, L.M., Wang, F.: Modular multilevel converters with integrated arm inductors for high quality current waveforms. In: Proceedings of IEEE ECCE Asia, pp. 636–642 (2013)
27. Kucka, J., Karwatzki, D., Baruschka, L., Mertens, A.: Modular multilevel converter with magnetically coupled inductors. IEEE Trans. Power Electron. **32**(9), 6767–6777 (2017)
28. Le, D.D., Lee, D.-C.: Integration of coupled inductors for compact design of flying-capacitor modular multilevel converters. In: Proceedings of IEEE ECCE, pp. 5922–5927 (2019)
29. McLyman, C.: Transformer and Inductor Design Handbook, vol. 10. CRC Press, Boca Raton (2011)
30. Hitachi Metals: Selection and Use Directions for Magnet Wire. https://www.hitachimetals.co.jp/e/products/auto/el/pdf/MagnetWire_en.pdf (2019). Accessed 17 June 2019

Duc Dung Le received his B.S degree in Electrical Engineering from Ho Chi Minh City University of Technology, Ho Chi Minh City, Vietnam, in 2013. He is presently working towards his Ph.D. degree in the Department of Electrical Engineering, Yeungnam University, Gyeongsan, Korea. His current research interests include multi-level converters and DC microgrids.

Dong-Choon Lee received his B.S., M.S. and Ph.D. degrees in Electrical Engineering from Seoul National University, Seoul, Korea, in 1985, 1987 and 1993, respectively. He was a Research Engineer for Daewoo Heavy Industry, Korea, from 1987 to 1988. He has been a faculty member in the Department of Electrical Engineering, Yeungnam University, Gyeongsan, Korea, since 1994. He was a Visiting Scholar in the Power Quality Laboratory, Texas A&M University, College Station, TX, USA, in 1998; the Electrical Drive Center, University of Nottingham, Nottingham, ENG, UK, in 2001; the Wisconsin Electric Machines and Power Electronics Consortium, University of Wisconsin, Madison, WI, USA, in 2004; and the FREEDM Systems Center, North Carolina State University, Raleigh, NC, USA, from September 2011 to August 2012. He served as the Editor-in-Chief of the *Journal of Power Electronics* of the Korean Institute of Power Electronics (KIPE), from January 2015 to December 2017. In 2019, he served as the President of KIPE. His current research interests include power converter design and control, renewable energy and its grid connection, AC machine drives, and DC power system.

Heung-Geun Kim was born in Busan, South Korea, in 1956. He received the B.S., M.S. and Ph.D. degrees in Electrical Engineering from Seoul National University, Seoul, South Korea, in 1980, 1982 and 1988, respectively. Since 1984, he has been with the Department of Electrical Engineering, Kyungpook National University, Daegu, South Korea, where he is currently a Full Professor and the Director of the Microgrid Research Center. From 1990 to 1991, he was a Visiting Scholar with the Department of Electrical and Computer Engineering, University of Wisconsin-Madison, Madison, WI, USA. From 2006 to 2007, he was with the Department of Electrical Engineering, Michigan State University, East Lansing, MI, USA. His current research interests include ac machine control, photovoltaic power generation and microgrid systems.